

Valley-dependent Corner States in Honeycomb Photonic Crystal without Inversion Symmetry

HUYEN THANH PHAN,^{1,*} FENG LIU,^{2,3,4,**} KATSUNORI WAKABAYASHI^{1,5,6,***}

¹Department of Nanotechnology for Sustainable Energy, School of Science and Technology, Kwansai Gakuin University, Gakuen 2-1, Sanda, Hyogo 669-1337, Japan

²School of Physical Science and Technology, Ningbo University, Ningbo, 315-211, China

³Institute of High Pressure Physics, Ningbo University, Ningbo, 315-211, China

⁴Laboratory of Clean Energy Storage and Conversion, Ningbo University, Ningbo, 315-211, China

⁵Center for Spintronics Research Network (CSRN), Osaka University, Toyonaka 560-8531, Japan

⁶National Institute for Materials Science (NIMS), Namiki 1-1, Tsukuba 305-0044, Japan

*phanthanhhuyenpth@gmail.com

**liufeng@nbu.edu.cn

***waka@kwansai.ac.jp

Abstract: We study topological states of honeycomb photonic crystals in absence of inversion symmetry using plane wave expansion and finite element methods. The breaking of inversion symmetry in honeycomb lattice leads to contrasting topological valley indices, i.e., the valley-dependent Chern numbers in momentum space. We find that the topological corner states appear for 60° degree corners, but absent for other corners, which can be understood as the sign flip of valley Chern number at the corner. Our results provide an experimentally feasible platform for exploring valley-dependent higher-order topology in photonic systems.

© 2021 Optical Society of America under the terms of the [OSA Open Access Publishing Agreement](#)

1. Introduction

The application of mathematical concept, *topology*, to solid-state physics [1–4] has resulted in fruitful achievements to design functional quantum materials and devices [5–12]. For example, in topological insulators, owing to the nontrivial topological invariant of bulk wave functions, topologically protected edge states appear and provide robust electronic conduction even in the presence of local perturbations such as defects and edge roughness. Those topologically protected surface states are promising candidates for ultra low-power-consumption electronics and quantum computation [13]. Furthermore, not only the topologically protected edge states, the topologically protected corner states were recently found as a consequence of higher-order topology of bulk wavefunction [14–16]. Inspired from the topological materials, the concept of topology has been extended to the photonic crystals (PhCs) and intensively studied [17–20]. PhCs are artificially periodic structures that consist of dielectric media and meta-materials, where the electro-magnetic (EM) waves are described by Bloch functions similar to electron waves in crystalline materials. As analogies of insulators, dielectric PhCs can also prevent EM wave of certain frequencies from propagating through the periodic structure, resulting in the formation of photonic energy band gaps.

Since it is demanded to design and fabricate the photonic devices to provide lossless EM flow for the application of optical telecommunication and computing, studies of topological PhCs have drawn much attention and grown rapidly. Shortly after the theoretical proposal [21], the topologically protected unidirectional propagation of EM waves has been experimentally observed using two-dimensional (2D) magneto-optical PhCs in microwave regime [22, 23]. The research has stimulated further theoretical works on the PhCs waveguides [24–26] and also experimental studies on topological edges states in PhCs [27, 28]. Besides, the photonic analogy

of topological electronic materials has been realized such as the photonic Chern insulator [29,30] as a result of the broken time-reversal symmetry. In this system, Berry curvature has non-zero distribution in the momentum space, leading to non-zero Chern number after integrating Berry curvature over the momentum space. Moreover, even in the absence of Berry curvature, topological properties of PhCs can still be found in 2D square PhCs [31–34]. The photonic band structures of zero Berry curvature systems show the topologically non-trivial band gaps and the localization of EM wave at one-dimensional (1D) edges and zero-dimensional (0D) corners were also observed [32, 33]. These topological states are explained by vectored Zak phase and gapped Wannier bands [35–38], unlike Chern number in previous cases. Not only Chern number and Zak phase, the internal degree of freedoms like valley indices can also be used to characterize topological properties. Valley means the local minima or maxima of energy band structures. For example, graphene, which provides honeycomb network of π -electrons, has such valley structures at Dirac points in momentum space, which appear at non-equivalent K and K' points in the 1st BZ. In graphene, these valley indices work as pseudo-spin degree of freedom and can be detected through valley Hall effect [39]. In analogy to graphene, valley-Hall effect can also be explored in photonic systems [40–44], where it can explain for not only the first order topological states but also higher-order topology in photonic systems.

In this paper, we theoretically study the topological states of 2D honeycomb PhC without inversion symmetry, where two kinds of dielectric rods are placed to form the honeycomb lattice in air. Owing to the broken inversion symmetry, the system has non-equivalent valley degrees of freedom in momentum space. Therefore, Berry curvatures have non-zero distribution in momentum space, leading to the non-trivial topological indices [45–48]. The appearance of topological corner states as higher order topology are the results of interactions between non-equivalent valleys in honeycomb PhC. Our results suggest a promising platform of future experimental studies to explore valley dependence of higher-order topology in photonic systems and provide the possibility to the application of topological PhCs in optical communication using valley degree of freedoms.

2. 2D Honeycomb PhC with broken inversion symmetry and valley Chern number

Here we briefly give an overview of photonic states in 2D honeycomb PhC with broken inversion symmetry and introduce the valley Chern number. Figure 1(a) shows the lattice structure of 2D honeycomb PhC, where the solid rhombus indicates the unit cell. There are two non-equivalent lattice sites called A and B in the unit cell, where the radii for cylinders A and B are defined as r_A and r_B , respectively. Throughout this paper, we assume that the dielectric cylinders are Yttrium Iron Garnet (YIG) with dielectric constant $\varepsilon = 15$, and those are arranged periodically in honeycomb lattice with the period of a_0 in air. The eigenvalue equation for EM wave in periodic media is given as follow:

$$\frac{1}{\varepsilon(\mathbf{r})} \nabla \times \nabla \times \mathbf{E}(\mathbf{r}) = \frac{\omega^2}{c^2} \mathbf{E}(\mathbf{r}), \quad (1)$$

where $\mathbf{E}(\mathbf{r})$ is vector electric field and $\varepsilon(\mathbf{r})$ is dielectric function. $\mathbf{r} = (x, y)$ is the position vector in 2D space. We assume that the perpendicular direction to the 2D plane is translational invariant. c is the speed of light. ω is the eigenfrequency. Figure 1(b) shows the corresponding 1st Brillouin Zone (BZ) for 2D honeycomb PhC.

In Fig. 1(c), photonic band structure is shown for $r_A = r_B = 0.18a_0$. In this case, the system preserves inversion symmetry and becomes the photonic analogue of graphene. We calculate the photonic band structure by using the plane wave expansion method [49]. Here the unit of angular frequency is $2\pi c/a_0$. As we can see, the linear Dirac dispersion appears at K and K' points. In this sense, the present system can be considered as the photonic analog of graphene.

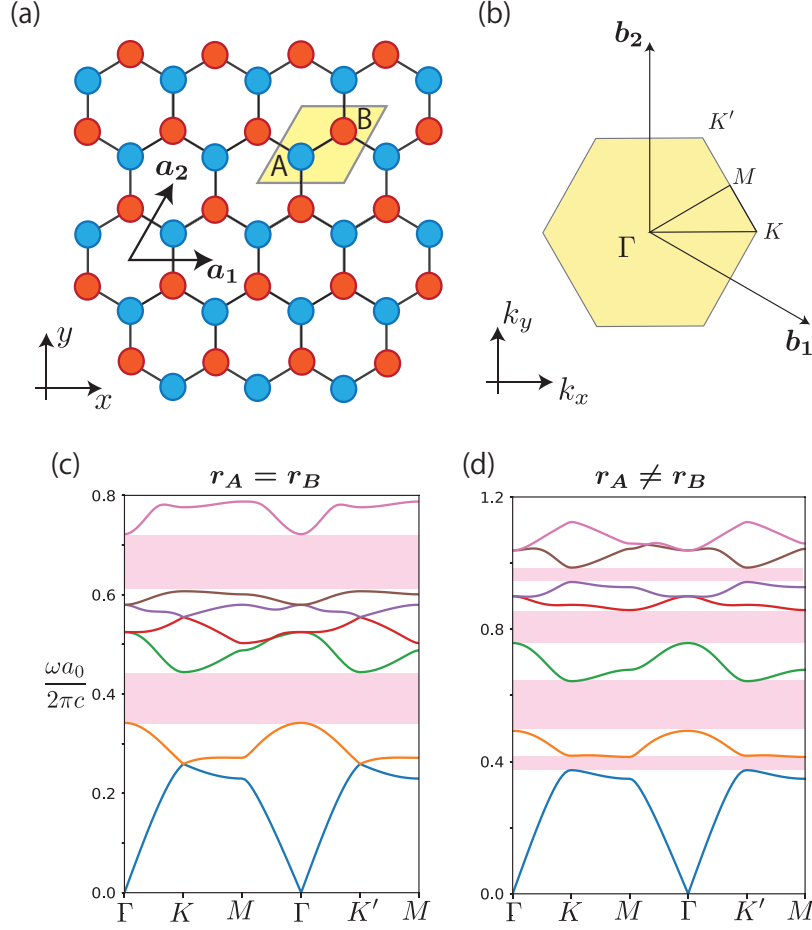


Fig. 1. (a) Schematic of 2D honeycomb PhC. $\mathbf{a}_1 = a_0(1, 0)$ and $\mathbf{a}_2 = a_0(1/2, \sqrt{3}/2)$ are primitive vectors. Here, a_0 is the lattice constant. Solid yellow rhombus indicates the primitive unit cell, which contains two non-equivalent dielectric rods called A and B, colored with cyan and magenta, respectively. The radii for these rods are r_A and r_B , respectively. (b) The corresponding 1st BZ of 2D honeycomb lattice with high symmetric points. \mathbf{b}_1 and \mathbf{b}_2 are primitive reciprocal lattice vectors. (c) Photonic band structure for 2D honeycomb PhC which conserves inversion symmetry ($r_A = r_B = 0.18a_0$), showing the Dirac points at K and K' point. (d) Photonic band structure for PhC with broken inversion symmetry $r_A = 0.0825a_0$ and $r_B = 0.1a_0$.

However, the complete photonic band gaps are opened around the frequencies of 0.4 and 0.65, which are intrinsic feature of 2D honeycomb PhCs.

Next we shall consider the case of broken inversion symmetry by making two rods different radii, i.e., $r_A \neq r_B$. Figure 1(d) shows the photonic band structure with broken inversion symmetry, i.e., $r_A = 0.0825a_0$ and $r_B = 0.1a_0$. Compared with the photonic band structure in Fig. 1(c), the degeneracies at Dirac points K and K' are lifted, leading to the complete band gaps with parabolic dispersion. This is the photonic analogue of electronic states for hexagonal Boron-Nitride (*hBN*). In this paper, we mainly focus on the 1st lowest photonic band gap, which originates from lifting the degeneracy at Dirac points between the 1st and the 2nd lowest photonic bands.

In Fig. 2(a), the evolution of eigenfrequency for the seven lowest EM modes is shown at high symmetric points Γ , K and M in the 1st BZ, where the rods radii r_A and r_B are varied. However, it is assumed that the sum of r_A and r_B is kept constant, i.e., $r_A + r_B = 0.183a_0$. It should be noted that the band inversions between 1st and 2nd, between 4th and 5th, and between 6th and 7th photonic subbands happen at K point when $r_A = r_B$. The band inversion indicates the topological phase transition of bulk EM waves.

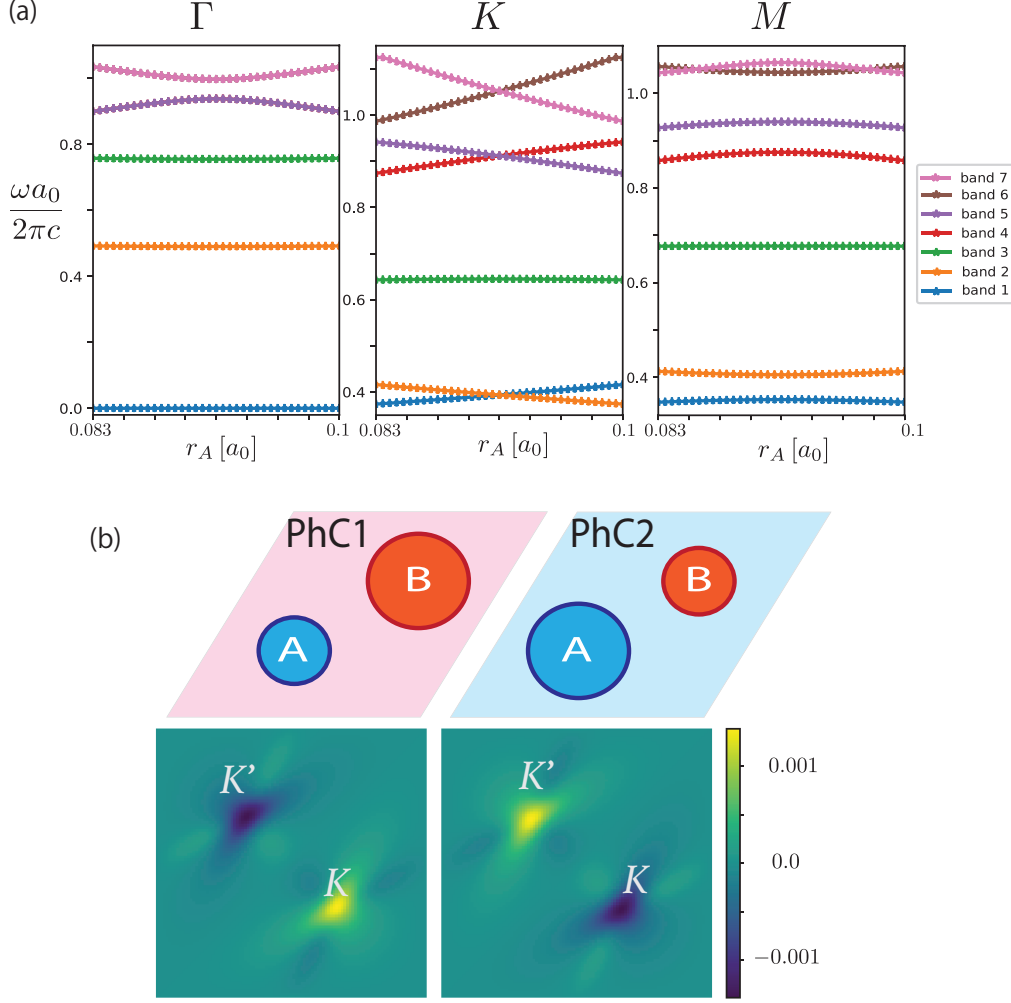


Fig. 2. (a) The radius size dependence of eigenfrequency for the seven lowest EM modes at high symmetric points, where the sum of r_A and r_B is kept constant, i.e., $r_A + r_B = 0.183$. (b) Two inverted PhC structures and their corresponding Berry curvature distribution in the 1st BZ. PhC2 is obtained by exchanging the position of two rods of PhC1.

From Fig. 2(a), we can also confirm that photonic band structure remains unchanged even if r_A and r_B are exchanged. Because of this symmetric property, we consider two inverted PhC structures as shown in Fig. 2(b). Let us define PhC with $r_A < r_B$ as PhC1, and PhC with $r_A > r_B$ as PhC2, respectively. These two PhC structures share the same photonic band structure given in Fig. 1(d). However, as can be seen above, the Berry curvature distribution in momentum space becomes different between PhC1 and PhC2.

In the broken inversion symmetry systems, the topological transition can be characterized by

the Berry curvature distribution in \mathbf{k} -space, i.e.,

$$\mathbf{\Omega}_n(\mathbf{k}) = \nabla_{\mathbf{k}} \times \mathbf{A}_n(\mathbf{k}), \quad (2)$$

where $\mathbf{A}_n(\mathbf{k}) = i \langle u_{n,\mathbf{k}} | \nabla_{\mathbf{k}} | u_{n,\mathbf{k}} \rangle$ is Berry connection and $|u_{n,\mathbf{k}}\rangle$ is periodic Bloch function of electric field. Owing to the broken inversion symmetry, the Berry curvature in the 1st BZ has opposite sign between K and K' points as indicated in Fig. 2(b). For PhC1, Berry curvature distribution around K point have positive value, however, that around K' point have the same magnitude but negative sign, i.e., $\mathbf{\Omega}_n(\mathbf{K}) = -\mathbf{\Omega}_n(\mathbf{K}')$. In further, PhC2 has reversed Berry curvature distribution compared with PhC1, i.e., $\mathbf{\Omega}_n(\mathbf{k})|_{PhC1} = -\mathbf{\Omega}_n(\mathbf{k})|_{PhC2}$. Since the 1st BZ is closed, the integration of Berry curvature over the 1st BZ is quantized in the unit of 2π [50]. Therefore, Chern number for a 2D closed surface is defined as

$$C_n = \frac{1}{2\pi} \iint_{BZ} \mathbf{\Omega}_n(\mathbf{k}) d^2k. \quad (3)$$

As can be seen in lower panel of Fig. 2(b), $\mathbf{\Omega}_n(\mathbf{k})$ has large values at K and K' points which give the large weight for this integration. Since Berry curvatures at K and K' points have opposite sign, Chern number is identically 0. However, if we focus on one of two Dirac points, Chern number is not zero. Thus, we shall introduce the valley Chern number as

$$C_n^\mu = \frac{1}{2\pi} \iint_{S_\mu} \mathbf{\Omega}_n(\mathbf{k}) d^2k, \quad (4)$$

where $\mu = K, K'$. The integration area S_μ indicates the $\frac{1}{2}$ of 1st BZ which includes only K or K' point.

3. Topological interface states

In this section, we discuss the localization of EM waves at 1D zigzag interface between PhC1 and PhC2. The total Chern number of the 1st band for both PhC1 and PhC2 is 0, because each of PhCs preserves time reversal symmetry [51]. However, the valley Chern number at each valley has non-zero value, which is similar to ref. [52]. In details, the valley Chern number for PhC1 is $C_1^K|_{PhC1} = 1/2$, $C_1^{K'}|_{PhC1} = -1/2$ and for PhC2 is $C_1^K|_{PhC2} = -1/2$, $C_1^{K'}|_{PhC2} = 1/2$.

According to the simple theoretical observations, at the interface between PhC1 and PhC2, the valley Chern number for each K points is quantized as:

$$\Delta C^K = C_1^K|_{PhC1} - C_2^K|_{PhC2} = 1/2 - (-1/2) = 1, \quad (5)$$

$$\Delta C^{K'} = C_1^{K'}|_{PhC1} - C_2^{K'}|_{PhC2} = -1/2 - 1/2 = -1. \quad (6)$$

Thus, K and K' valleys have quantized Chern number with opposite sign, which leads to topological phase transition at the interface between PhC1 and PhC2. As a consequence of topological phase transition, highly localized EM states appear at the interface, i.e., topological interface (edge) states. Such topological interface EM states propagates along the interface and quite robust against the scattering from interface roughness and crystal defects.

In the left panels of Figs. 3(a) and (b), two different types of interface structure between PhC1 and PhC2 are shown. We call them the interface A and B, respectively. For the interface A, PhC2 is placed upper semi-half region, but PhC1 is placed lower semi-half region. In this case, larger dielectric cylinders come to at the interface. For the interface B, the regions for PhC1 and PhC2 are inverted, then, smaller dielectric cylinders come to at the interface. Here the interface is taken along the zigzag edge direction of 2D honeycomb lattice, i.e., the interface has the

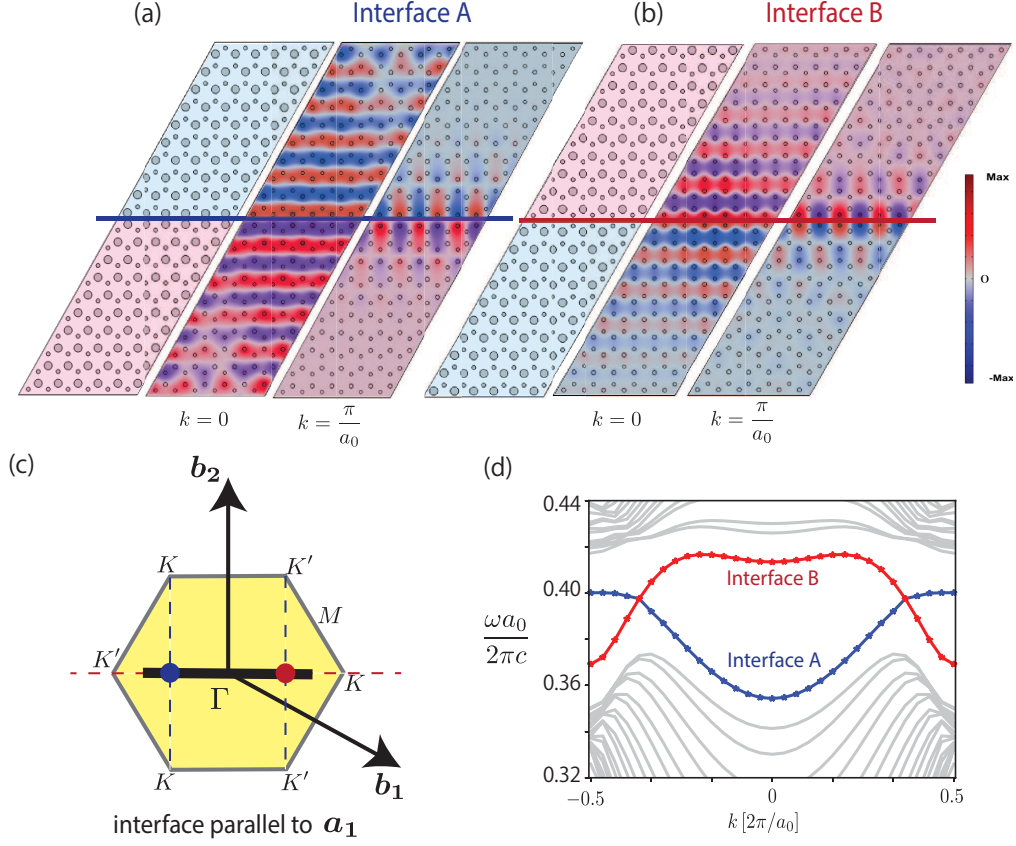


Fig. 3. The schematic of zigzag interface type A (a) and interface type B (b) between PhC1 and PhC2 (left panels), which has the translational invariance along both \mathbf{a}_1 and \mathbf{a}_2 directions. The corresponding field profile of each interface structure at $k = 0$ (middle panels) and $k = \frac{\pi}{a_0}$ (right panels). Magenta regions indicate PhC1 and cyan regions indicate PhC2. (c) The corresponding 1st BZ (thick black line) for the interface structure which is parallel to \mathbf{a}_1 direction. Blue (red) dot indicates the projection of K (K') points on to the 1st BZ. (d) Photonic band structure for the interface structure near the 1st photonic band gap. Gray lines are bulk states. The blue line is the interface states for the interface A. The red line is the interface states for the interface B.

translational invariance along \mathbf{a}_1 direction. To distinguish between interfaces A and B, we shall define the valley Chern number for interface as follows:

$$C_A^K := C_1^K |_{\text{PhC2}} - C_2^K |_{\text{PhC1}} = -1/2 - 1/2 = -1, \quad (7)$$

$$C_A^{K'} := C_1^{K'} |_{\text{PhC2}} - C_2^{K'} |_{\text{PhC1}} = 1/2 - (-1/2) = 1, \quad (8)$$

$$C_B^K := C_1^K |_{\text{PhC1}} - C_2^K |_{\text{PhC2}} = 1/2 - (-1/2) = 1, \quad (9)$$

$$C_B^{K'} := C_1^{K'} |_{\text{PhC1}} - C_2^{K'} |_{\text{PhC2}} = -1/2 - 1/2 = -1. \quad (10)$$

Here, we have defined the valley Chern number of $\alpha (= K, K')$ valley for the interface $\beta (= A, B)$ as C_β^α . It should be noted that the valley Chern numbers satisfy the following relations:

$$C_A^\alpha = -C_B^\alpha, \quad (11)$$

$$C_\beta^K = -C_\beta^{K'}. \quad (12)$$

In the middle and right panels of Figs. 3(a) and (b), the spatial distribution of electric field is shown at $k = 0$ and $k = \pi/a_0$, respectively. Owing to the presence of finite valley Chern number, the localized EM states are observed along the interfaces. Electric field is highly localized at the domain wall between two PhCs at $k = \pi/a_0$ and much more penetrate into the bulk at $k = 0$. It should be also noted that EM waves of interface states have opposite group velocities near K and K' points between interfaces A and B, which can be confirmed from the photonic band structure shown in Fig.3(d).

In Fig. 3(c), the projected 1st BZ for interface structures is denoted as a thick black line. The K and K' points are projected to $-\pi/3a_0$ and $\pi/3a_0$, respectively. The photonic energy band structure for interfaces A and B is shown in Fig. 3(d). The blue line is the interface states for the interface A, while the red line is the interface states for interface B. Grey lines represent bulk states originated from 1st and 2nd subbands. It is clearly observed that topological interface states appear inside photonic bandgap for bulk PhC as being observed before in [52]. However, while only one type of interface structure were examined in [52], our results show two possible zigzag interface structures, which are created from PhC1 and PhC2.

4. Topological corner states

Recently, the localization of EM wave at 0D corners, so-called corner states, as higher-order topology were examined in several PhC structures, where the topological corner states are explained by vectored Zak phase and gapped Wannier bands [35–37]. Here we show that the localized EM corner states can occur even in the honeycomb PhC with broken inversion symmetry. We will see that selection rule of corner state formation in the present system, i.e. corner states appear for 60° corner, but absent for 120° corner. This selection rule can be elucidated as the consequence of valley-valley interaction.

To observe corner states, we consider triangular PhC structure in which another type triangular PhC is embedded. Figures 4 (a) and (b) show such triangular PhCs. In Fig. 4(a), triangular PhC2 is embedded in the triangular PhC1. In this case, the interface between PhC1 and PhC2 becomes the interface A, hereafter, we call triangular PhC-A. Figure 4(b) shows another type of triangular PhC, where PhC1 is embedded in PhC2. In this case, the interface between PhC1 and PhC2 becomes the interface B, so similarly we call triangular PhC-B hereafter. Both of structures have three 60° corners. To implement the numerical calculations, the perfect electric conductor (PEC) boundary condition is imposed for outside triangular PhCs. The structure contains 20 lattice sites for inner triangular PhC, and 32 lattice sites for outer triangular PhC.

Figures 4(c) shows the photonic angular frequency spectrum of triangular PhC-A. The red dots indicate the eigenfrequencies of three corner states. Figures 4(d) shows the field profile for each corner state. Electric field of each corner state is localized at one of two sublattices at the corners, then decays exponentially.

Similarly, Figure 4(e) shows the photonic angular frequency spectrum of triangular PhC-B, where the red dots indicate the corner states. In this case, three corner states appear inside the photonic band gap, i.e., well-separated from bulk and interface states. Figure 4 (f) show the field profile for each corner states.

It can be seen that the corner states of triangular PhC-A are mixed with bulk and edges states. But the corner states of triangular PhC-B are isolated. This difference can be understood by inspecting the photonic band structure for the interface structures A and B as shown in Fig. 3 (d). The frequency range of interface A is completely overlapped with that of bulk and interface B. However, in the frequency range from 0.4 to 0.415, only interface B states are found. In the triangular structure, there are three outside edges with PEC boundary condition, so-called PEC edges. For triangular PhC-A, the PEC edges have the same structure as interface B. Therefore, in the gap of bulk photonic band, we find no frequency range of only interface A, resulting in the mixing the corner states with the bulk and PEC edges states. For triangular PhC-B, the PEC

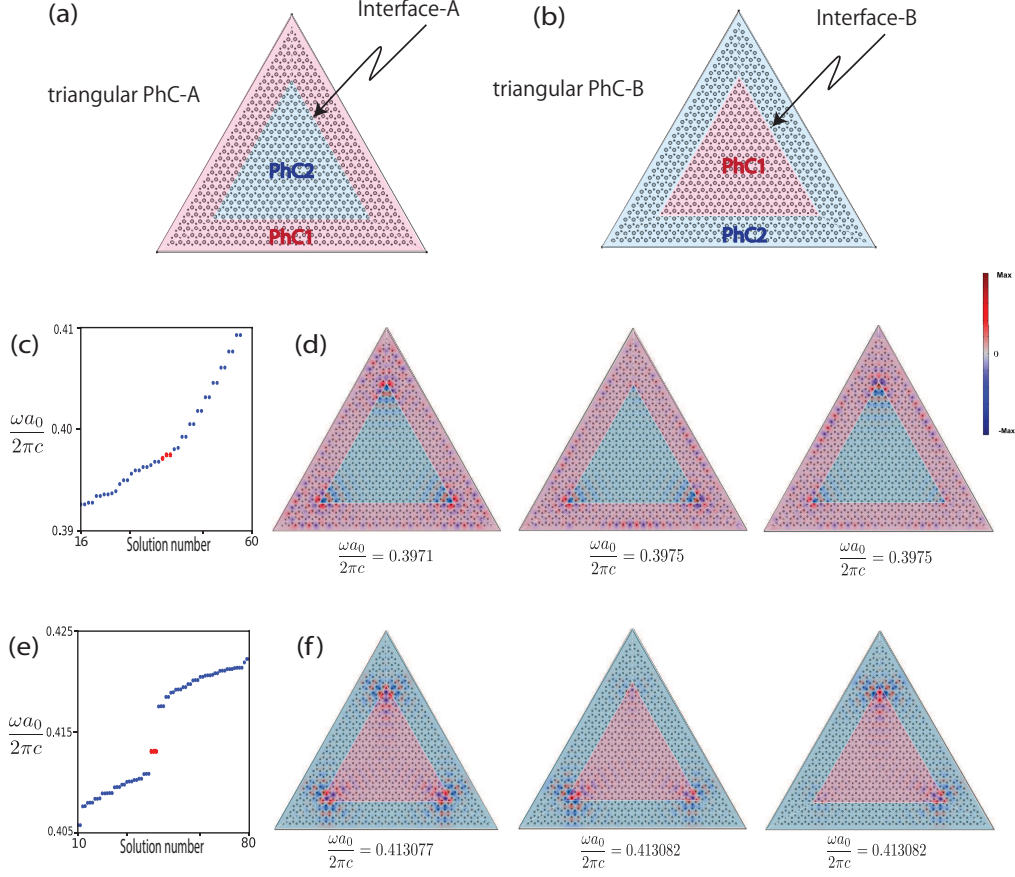


Fig. 4. (a) Structure of triangular PhC-A. The triangular PhC2 is embedded inside triangular PhC1, in which the interface structure becomes interface A. (b) Structure of triangular PhC-B. Compared with PhC-A, PhC1 and PhC2 are mutually replaced. The interface structure is interface B. (c) Photonic angular frequency spectrum of triangular PhC-A. The red dots indicate of eigenfrequencies for corner states. Three corner states appear. (d) Electric field profile of three corner states for triangular PhC-A. (e) Photonic angular frequency spectrum of triangular PhC-B. (f) Electric field profile of three corner states for triangular PhC-B.

edges have the same structure as interface A. In the frequency range from 0.4 to 0.415, there are only the states of interface B. Therefore, the corner states of triangular PhC-B are isolated from bulk and PEC edge states.

The eigenfrequencies of three corner states in both cases are mutually close. But, one of them is slightly lower than others. This is due to the interaction between three corner states. This behavior can be understood by employing simple three-sites tight-binding model. Let us represent the spatially localized electric field at three corners as ϕ_1 , ϕ_2 and ϕ_3 , respectively. Then, we shall assume that these three spatially localized electric fields mutually interfere with the strength of $-\gamma$. Here, γ is a parameter to represent the strength of interference and minus sign indicates that the constructive interference makes energy lower. So then, we can construct effective tight-binding Hamiltonian as

$$H = -\gamma (|\phi_1\rangle\langle\phi_2| + |\phi_2\rangle\langle\phi_3| + |\phi_3\rangle\langle\phi_1|) + \text{H.c.} \quad (13)$$

This three-sites model gives three eigenvalues as -2γ , γ , γ , i.e., two of them are degenerate. The

corresponding eigenvectors are $(\phi_1, \phi_2, \phi_3) = (1, 1, 1)$, $(1, 0, -1)$ and $(-1, 1, 0)$, respectively. Thus, as shown in the Figs. 4(e) and (g), three corner states have almost same amplitudes at the corners, but in middle and right panels, one of corner states is missing.

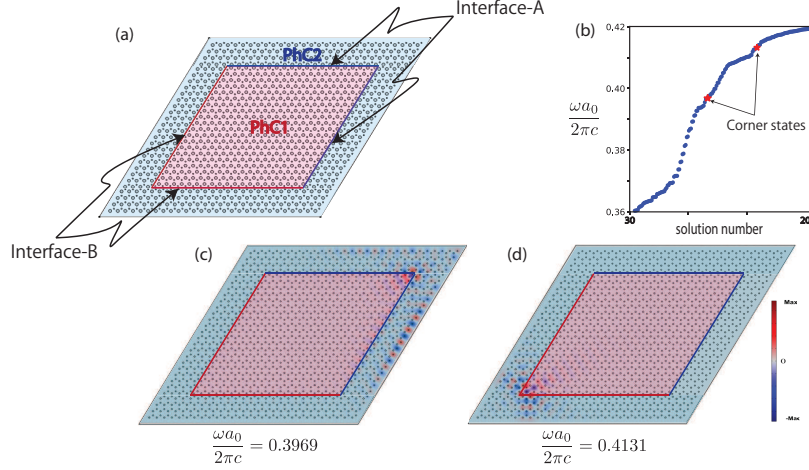


Fig. 5. (a) Rhombus structure of PhC1 and PhC2, consisting of both interface A (blue lines) and interface B (red lines). (b) The frequency spectrum for the rhombus structure. Red dots indicate the frequencies of 60° corner states. The corresponding field profile of 60° corner states which is form by interface A (c) and interface B (d).

We also examined another structure, which includes both 60° and 120° corners as shown in Fig. 5(a). The blue and red lines denote the interface A and interface B. The structure has the size of 28×28 supercell of PhC2. Inside the PhC2, PhC1 with the supercell of 20×20 is embedded. PEC boundary condition has been imposed for the outer surface of PhC2 for numerical calculation. Figure 5(b) shows the photonic spectrum of the rhombus structure. The red dots indicate frequencies for the states where electric field is localized at the 60° corners. The corner state with lower frequency has the field profile shown in Fig. 5(c). This state is slightly mixed with the interface states. The corner state with higher frequency has the field profile shown in Fig. 5(d). This corner state is isolated from other interface and bulk states. These results matches with the cases of triangular structures. As for the 120° corner, localized corner states are absent.

Now we elucidate why the topological corner states appear at 60° corner, but absent in 120° corner. In previous section, we have considered the zigzag interfaces which are parallel to \mathbf{a}_1 direction shown in Figs. 3(a) and (b). In similar manner, we can also build the zigzag interfaces which are parallel to either \mathbf{a}_2 or \mathbf{a}_3 direction. The black bold lines in Fig. 6(a) indicate the 1D 1st BZ of projected band structure for zigzag interface in \mathbf{a}_1 , \mathbf{a}_2 and \mathbf{a}_3 directions. The blue and red arrows indicate group velocity direction at each valley of interface A and interface B, respectively. The group velocity v_g is given by $v_g = \nabla_{\mathbf{k}} \omega(\mathbf{k})$. Figure 6 (b) is the schematic of 60° corner, which includes two interfaces A or two interfaces B. EM waves of interface states propagating toward the corner belong to different valley. Thus, 60° corners always connect two interfaces with different valley Chern number, i.e., the formation of corner states at 60° corners. On the other hand, Figure 6 (c) is the schematic of 120° corner, which includes both interface A and interface B. In this case, EM waves propagating toward the corner belong to the mutually opposite valley. However, since the valley Chern number are opposite between interfaces A and B (see Eq.(12)), 120° corners connect two interfaces with same valley Chern number, i.e., no formation of corner states at 120° corner. Thus, the sign flip of valley Chern numbers is necessary condition of corner state formation.

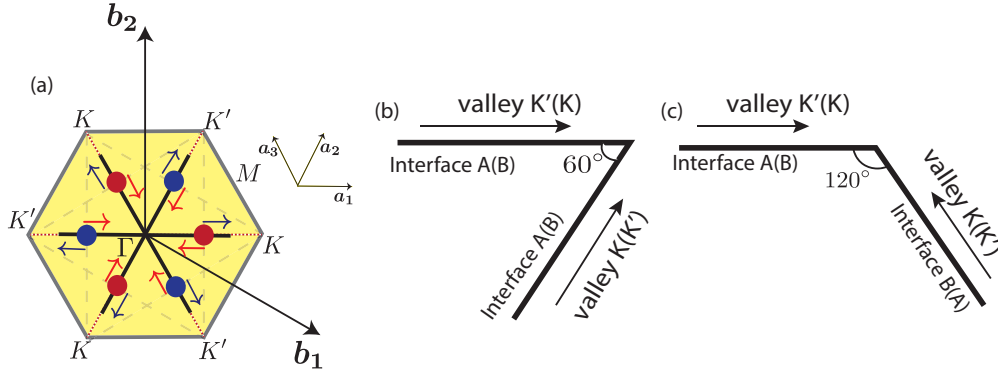


Fig. 6. (a) The 1st BZ (thick black lines) for the interface structures which are parallel to \mathbf{a}_1 , \mathbf{a}_2 and \mathbf{a}_3 directions. The blue and red circles indicate the projection of K and K' points on to the 1st BZ. Blue and red arrows indicate the directions of group velocity at each valley for interface A and interface B, respectively. (b) Schematic structure of 60° corner, which connect two interfaces with same type. (c) Schematic structure of 120° corner, which connect two interfaces with different type.

The 60° corners connect two interfaces with the opposite valley Chern number, but 120° corners connect two interfaces with the same valley Chern number. Thus, the angle-dependent formation of corner states are attributed to the valley Chern number. To describe this, we shall introduce the pseudo-spin for valley Chern number. In the following, we assume that the valley Chern number 1 is pseudo-spin up and the valley Chern number -1 is pseudo-spin down. The two interfaces of 60° corner will have the interaction between two different valleys, which can be understood by the coupling of pseudo-spin up and pseudo-spin down. However, for the 120° corner, two interfaces show the same valley Chern number. Therefore, there is no interaction between two interfaces of 120° corner.

To formulate this argument for the corner states, we introduce the pseudo-spin states as $|\uparrow\rangle = (1, 0)^T$, $|\downarrow\rangle = (0, 1)^T$ to represent valley Chern number $C = 1$ and -1 , respectively. Here we have omitted the valley and interface indices, because they are not relevant in the following. And, $(\dots)^T$ indicates the transpose of vector. Then we construct the general form of Hamiltonian, H_{corner} , to represent the formation of corner state as the interaction between two states with different valley Chern number, i.e.,

$$H_{\text{corner}} = \varepsilon_0 I + \nu k \sigma_z + m \sigma_x + m \sigma_y, \quad (14)$$

where ε_0 and ν are the eigenfrequency and group velocity at K and K' points, respectively. Here, I is unit matrix, σ_x , σ_y and σ_z are Pauli matrices, m is real value. Note that the group velocities have mutually opposite directions at K and K' points. The first two terms of H_{corner} give the diagonal part of Hamiltonian, which represents energy for each specific interface. Since valley Chern number at K and K' points are finite, we represent the interaction between the different valleys of two interfaces as the third and the fourth terms. The real value m shows the strength for the interaction, which depends on the structures and materials. The 60° corners have finite interaction between two interfaces, leading to the scattering between pseudo-spin states. On the other hand, for 120° corners, m should be zero, because there is no interaction between K and K' points, i.e., conservation of pseudo-spin state.

Finally we shall mention about other corner angles such as 30° , 90° , 150° . These corners are constructed as the combination of zigzag and armchair edges. Thus, the corners always contain an armchair edge. As for armchair edges, K and K' points come to $k = 0$ in the projected 1D 1st BZ, i.e., $\Delta C^K + \Delta C^{K'} = 0$. Thus, the valley Chern number becomes identically zero. Because

the sign change of valley Chern number are not involved at these corners, no corner state appears at 30° , 90° and 150° corners. It is noted that this observation is similar to the graphene corner states [53, 54], but where the formation mechanism of corner states relies on Zak phase, not valley Chern number.

5. Conclusion

In this paper, we have numerically studied the EM states in the honeycomb PhC structure using plane wave expansion and finite element methods. The system is composed of dielectric cylinders which are periodically arrayed on the honeycomb lattice. Owing to the honeycomb lattice symmetry, the unit cell contains two non-equivalent dielectric cylinders with the radii r_A and r_B .

In case of $r_A = r_B$, the system possesses inversion symmetry and becomes photonic analogue of graphene, i.e., Dirac cones at K and K' points in the 1st BZ. However, if two cylinders have different diameters, i.e., $r_A \neq r_B$, the inversion symmetry is broken, resulting in the lift of Dirac points in the photonic band structure, i.e., photonic bandgap opening. In this situation, K and K' points have finite Berry curvature but with opposite signs. Since the system respects with time-reversal symmetry, total Chern number is always zero. However, K and K' possess finite valley Chern number with mutually opposite sign.

The hidden topological properties of valley Chern number can be extracted by considering the interface between two different PhCs, where one side is PhC with $r_A > r_B$, the other side is $r_A < r_B$. Along the interface, we have found the formation of the interface states owing to the finite valley Chern number.

It is found that 60° corner structure can induce the localized corner states as a consequence of sign flip of valley Chern number at corners. However, such corner states are absent for 120° , because no sign flip of valley Chern number is involved. It is also pointed out the corners with 30° , 90° and 150° also do not possess the corner states, because these corner involves armchair edges where total valley Chern number identically zero.

Our results suggest the topological design of photonic crystal on the basis of valley degree of freedom. The topological interface states can be useful for the high efficient optical communication technology, and the corner states will be useful for the confinement of electromagnetic waves.

Acknowledgments

K.W. acknowledges the financial support by JSPS KAKENHI (Grant No. 21H01019 and JP18H01154), and JST CREST (Grant No. JPMJCR19T1). F. L. acknowledges the financial support by Research Starting Funding of Ningbo University and NSFC Grant No. 12074205.

Disclosures

The authors declare no conflicts of interest.

References

1. A. Bansil, H. Lin, and T. Das, "Colloquium: Topological band theory," *Rev. Mod. Phys.* **88**, 021004 (2016).
2. M. Z. Hasan and C. L. Kane, "Colloquium: Topological insulators," *Rev. Mod. Phys.* **82**, 3045–3067 (2010).
3. X.-L. Qi and S.-C. Zhang, "Topological insulators and superconductors," *Rev. Mod. Phys.* **83**, 1057–1110 (2011).
4. Y. Ando, "Topological insulator materials," *J. Phys. Soc. Jpn.* **82**, 102001 (2013).
5. B. A. Bernevig, T. L. Hughes, and S.-C. Zhang, "Quantum spin hall effect and topological phase transition in hgte quantum wells," *Science* **314**, 1757–1761 (2006).
6. M. Sato and S. Fujimoto, "Majorana fermions and topology in superconductors," *J. Phys. Soc. Jpn.* **85**, 072001 (2016).
7. L. Fu, C. L. Kane, and E. J. Mele, "Topological insulators in three dimensions," *Phys. Rev. Lett.* **98**, 106803 (2007).
8. C. L. Kane and E. J. Mele, "Quantum spin hall effect in graphene," *Phys. Rev. Lett.* **95**, 226801 (2005).

9. Y. L. Chen, J. G. Analytis, J.-H. Chu, Z. K. Liu, S.-K. Mo, X. L. Qi, H. J. Zhang, D. H. Lu, X. Dai, Z. Fang, S. C. Zhang, I. R. Fisher, Z. Hussain, and Z.-X. Shen, "Experimental realization of a three-dimensional topological insulator, Bi_2Te_3 ," *Science* **325**, 178–181 (2009).
10. M. Kim, J. Kim, Y. Hou, D. Yu, Y.-J. Doh, B. Kim, K. W. Kim, and J. Suh, "Nanomechanical characterization of quantum interference in a topological insulator nanowire," *Nat. Commun.* **10**, 4522 (2019).
11. R. Okuyama, W. Izumida, and M. Eto, "Topological classification of the single-wall carbon nanotube," *Phys. Rev. B* **99**, 115409 (2019).
12. D. Kong, J. C. Randel, H. Peng, J. J. Cha, S. Meister, K. Lai, Y. Chen, Z.-X. Shen, H. C. Manoharan, and Y. Cui, "Topological insulator nanowires and nanoribbons," *Nano Lett.* **10**, 329–333 (2010). PMID: 20030392.
13. M. He, H. Sun, and Q. L. He, "Topological insulator: Spintronics and quantum computations," *Front. Phys.* **14**, 43401 (2019).
14. M. Ezawa, "Higher-order topological insulators and semimetals on the breathing kagome and pyrochlore lattices," *Phys. Rev. Lett.* **120**, 026801 (2018).
15. M. Ezawa, "Topological switch between second-order topological insulators and topological crystalline insulators," *Phys. Rev. Lett.* **121**, 116801 (2018).
16. X.-W. Luo and C. Zhang, "Higher-order topological corner states induced by gain and loss," *Phys. Rev. Lett.* **123**, 073601 (2019).
17. H. Wang, S. K. Gupta, B. Xie, and M. Lu, "Topological photonic crystals: a review," *Front. Optoelectronics* **13**, 50–72 (2020).
18. L. Lu, J. D. Joannopoulos, and M. Soljačić, "Topological photonics," *Nat. Photon.* **8**, 821–829 (2014).
19. T. Ozawa, H. M. Price, A. Amo, N. Goldman, M. Hafezi, L. Lu, M. C. Rechtsman, D. Schuster, J. Simon, O. Zilberberg, and I. Carusotto, "Topological photonics," *Rev. Mod. Phys.* **91**, 015006 (2019).
20. Y. Ota, K. Takata, T. Ozawa, A. Amo, Z. Jia, B. Kante, M. Notomi, Y. Arakawa, and S. Iwamoto, "Active topological photonics," *Nanophotonics* **9**, 547–567 (2020).
21. F. D. M. Haldane and S. Raghu, "Possible realization of directional optical waveguides in photonic crystals with broken time-reversal symmetry," *Phys. Rev. Lett.* **100**, 013904 (2008).
22. Z. Wang, Y. D. Chong, J. D. Joannopoulos, and M. Soljačić, "Reflection-free one-way edge modes in a gyromagnetic photonic crystal," *Phys. Rev. Lett.* **100**, 013905 (2008).
23. Z. Wang, Y. Chong, J. D. Joannopoulos, and M. Soljačić, "Observation of unidirectional backscattering-immune topological electromagnetic states," *Nature* **461**, 772–775 (2009).
24. M. Hafezi, E. A. Demler, M. D. Lukin, and J. M. Taylor, "Robust optical delay lines with topological protection," *Nat. Phys.* **7**, 907–912 (2011).
25. A. B. Khanikaev, S. Hossein Mousavi, W.-K. Tse, M. Kargarian, A. H. MacDonald, and G. Shvets, "Photonic topological insulators," *Nat. Mater.* **12**, 233–239 (2013).
26. S. A. Skirlo, L. Lu, and M. Soljačić, "Multimode one-way waveguides of large chern numbers," *Phys. Rev. Lett.* **113**, 113904 (2014).
27. M. C. Rechtsman, J. M. Zeuner, Y. Plotnik, Y. Lumer, D. Podolsky, F. Dreisow, S. Nolte, M. Segev, and A. Szameit, "Photonic floquet topological insulators," *Nature* **496**, 196–200 (2013).
28. M. Hafezi, S. Mittal, J. Fan, A. Migdall, and J. M. Taylor, "Imaging topological edge states in silicon photonics," *Nat. Photonics* **7**, 1001–1005 (2013).
29. C. He, L. Lin, X.-C. Sun, X.-P. Liu, M.-H. Lu, and Y.-F. Chen, "Topological photonic states," *Int. J. Mod. Phys. B* **28**, 1441001 (2014).
30. Z. Wang, Y. D. Chong, J. D. Joannopoulos, and M. Soljačić, "Reflection-free one-way edge modes in a gyromagnetic photonic crystal," *Phys. Rev. Lett.* **100**, 013905 (2008).
31. F. Liu, H.-Y. Deng, and K. Wakabayashi, "Topological photonic crystals with zero berry curvature," *Phys. Rev. B* **97**, 035442 (2018).
32. Y. Ota, F. Liu, R. Katsumi, K. Watanabe, K. Wakabayashi, Y. Arakawa, and S. Iwamoto, "Photonic crystal nanocavity based on a topological corner state," *Optica* **6**, 786–789 (2019).
33. X. Zhang, H.-X. Wang, Z.-K. Lin, Y. Tian, B. Xie, M.-H. Lu, Y.-F. Chen, and J.-H. Jiang, "Second-order topology and multidimensional topological transitions in sonic crystals," *Nat. Phys.* **15**, 582–588 (2019).
34. X.-D. Chen, W.-M. Deng, F.-L. Shi, F.-L. Zhao, M. Chen, and J.-W. Dong, "Direct observation of corner states in second-order topological photonic crystal slabs," *Phys. Rev. Lett.* **122**, 233902 (2019).
35. P. Delplace, D. Ullmo, and G. Montambaux, "Zak phase and the existence of edge states in graphene," *Phys. Rev. B* **84**, 195452 (2011).
36. F. Liu, H.-Y. Deng, and K. Wakabayashi, "Helical topological edge states in a quadrupole phase," *Phys. Rev. Lett.* **122**, 086804 (2019).
37. W. A. Benalcazar, B. A. Bernevig, and T. L. Hughes, "Quantized electric multipole insulators," *Science* **357**, 61–66 (2017).
38. H. Xue, Y. Yang, F. Gao, Y. Chong, and B. Zhang, "Acoustic higher-order topological insulator on a kagome lattice," *Nat. Mater.* **18**, 108–112 (2019).
39. D. Xiao, W. Yao, and Q. Niu, "Valley-contrasting physics in graphene: Magnetic moment and topological transport," *Phys. Rev. Lett.* **99**, 236809 (2007).
40. Z. Gao, Z. Yang, F. Gao, H. Xue, Y. Yang, J. Dong, and B. Zhang, "Valley surface-wave photonic crystal and its

- bulk/edge transport.” *Phys. Rev. B* **96**, 201402 (2017).
41. J. Noh, S. Huang, K. P. Chen, and M. C. Rechtsman, “Observation of photonic topological valley hall edge states,” *Phys. Rev. Lett.* **120**, 063902 (2018).
 42. X. Zhang, M. Xiao, Y. Cheng, M.-H. Lu, and J. Christensen, “Topological sound,” *Commun. Phys.* **1**, 97 (2018).
 43. J. Lu, C. Qiu, W. Deng, X. Huang, F. Li, F. Zhang, S. Chen, and Z. Liu, “Valley topological phases in bilayer sonic crystals,” *Phys. Rev. Lett.* **120**, 116802 (2018).
 44. X. Ni, D. Purtseladze, D. A. Smirnova, A. Slobozhanyuk, A. Alù, and A. B. Khanikaev, “Spin- and valley-polarized one-way klein tunneling in photonic topological insulators,” *Sci. Adv.* **4** (2018).
 45. X.-L. Qi, T. L. Hughes, and S.-C. Zhang, “Topological field theory of time-reversal invariant insulators,” *Phys. Rev. B* **78**, 195424 (2008).
 46. D. N. Sheng, Z. Y. Weng, L. Sheng, and F. D. M. Haldane, “Quantum spin-hall effect and topologically invariant chern numbers,” *Phys. Rev. Lett.* **97**, 036808 (2006).
 47. K. Shiozaki and M. Sato, “Topology of crystalline insulators and superconductors,” *Phys. Rev. B* **90**, 165114 (2014).
 48. X.-Y. Dong and C.-X. Liu, “Classification of topological crystalline insulators based on representation theory,” *Phys. Rev. B* **93**, 045429 (2016).
 49. J. D. Joannopoulos, S. G. Johnson, J. N. Winn, and R. D. Meade, *Molding the flow of light* (Princeton University, 2008).
 50. M. Blanco de Paz, C. Devescovi, G. Giedke, J. J. Saenz, M. G. Vergniory, B. Bradlyn, D. Bercioux, and A. García-Etxarri, “Tutorial: Computing topological invariants in 2d photonic crystals,” *Adv. Quantum Technol.* **3**, 1900117 (2019).
 51. S. Raghu and F. D. M. Haldane, “Analogues of quantum-hall-effect edge states in photonic crystals,” *Phys. Rev. A* **78**, 033834 (2008).
 52. X.-D. Chen, F.-L. Zhao, M. Chen, and J.-W. Dong, “Valley-contrasting physics in all-dielectric photonic crystals: Orbital angular momentum and topological propagation,” *Phys. Rev. B* **96**, 020202 (2017).
 53. F. Liu and K. Wakabayashi, “Higher-order topology and fractional charge in monolayer graphene,” *Phys. Rev. Res.* **3**, 023121 (2021).
 54. Y. Shimomura, Y. Takane, and K. Wakabayashi, “Electronic states and local density of states in graphene with a corner edge structure,” *J. Phys. Soc. Jpn.* **80**, 054710 (2011).